ADVANCED HEALTHCARE MATERIALS
www.advhealthmat.de

Multivalent Protein Nanorings for Broad and Potent SARS-CoV-2 Neutralization

Molood Behbahanipour, Carla Goldin, Cecilia Arahi Prato, Ana Luz Paletta, Oriol Bárcenas, Susanna Navarro, Jordi Pujols, Daniel H. Murgida, María Virginia Tribulatti, Sebastián Esperante, Damian Alvarez-Paggi, and Salvador Ventura**

The ongoing threat of severe acute respiratory syndrome coronavirus 2 (SARS-CoV-2) and the limitations of conventional antibody-based therapeutics (ABTs) underscore the need for scalable and customizable antiviral platforms. A modular, protein-only nanoscaffold based on recombinant ring-like particles (RLPs) derived from a viral nucleoprotein (*NP*), engineered is presented to display high-affinity, de novo-designed minibinders (LCB1 and LCB3) targeting SARS-CoV-2 Spike (*S*)protein. These binders are site-specifically fused to either the N- or C-termini, or both ends of *NP* to ensure functional orientation and dense, multivalent display. The resulting constructs self-assemble into stable, biocompatible, and homogeneous nanoparticles that potently inhibit *S*–angiotensin-converting enzyme 2 receptor (ACE2r) interactions, neutralizing both pseudotyped viral-like particles and authentic SARS-CoV-2, including Omicron BA.5. The dual-display nanoparticle (RLP-1,3), presenting 10 LCB1 and 10 LCB3 domains, exhibit synergistic binding activity, with fM Half Maximal Inhibitory Concentration(IC_{50}) values, outperforming benchmark monoclonal antibodies and clinically approved hyperimmune therapies. Additionally, RLP-1,3 is adapted for diagnostics in an ELISA platform, achieving a Spike protein detection limit of 9 ng mL^{-1}, surpassing commercial assays. This work demonstrates how the convergence of AI-guided binder design and structure-based nanoscaffolding enables next-generation multifunctional bio-nanomaterials. The RLP-minibinder system offers a generalizable, scalable, and cost-efficient plug-and-(dis)play solution with integrated therapeutic and diagnostic capabilities, positioning it as a flexible alternative to ABTs for pandemic preparedness.

1. Introduction

The global burden of coronavirus disease 2019 (COVID-19) extends well beyond those infected and suffering respiratory symptoms to include individuals diagnosed with long COVID,[1] a condition characterized by persistent symptoms following initial recovery. As of April 2024, over 700 million confirmed COVID-19 cases have been reported worldwide, with the cumulative economic toll of the pandemic estimated in the tens of trillions of dollars.[2]

While vaccine development advanced at an unprecedented pace during the pandemic, largely driven by a convergence of emerging technologies and decades of foundational research in structural vaccinology[3–5] and coronavirus-related virology,[6] the development of effective therapeutics lagged behind. Antibodies-based therapeutic strategies (ABTs), involving either i) convalescent plasma donors,[7,8] ii) monoclonal antibodies (mAbs)[9–12] or iii) heterologous serotherapies such as hyperimmune equine sera (HES),[13,14] have been at the forefront of therapies for neutralizing severe acute respiratory syndrome coronavirus 2 (SARS-CoV-2).[15,18] However, the clinical efficacy

M. Behbahanipour, O. Bárcenas, S. Navarro, J. Pujols, S. Ventura
Institut de Biotecnologia i de Biomedicina (IBB) and Departament de Bioquímica i Biologia Molecular
Universitat Autònoma de Barcelona
Bellaterra (Barcelona) 08193, Spain
E-mail: salvador.ventura@uab.cat

The ORCID identification number(s) for the author(s) of this article can be found under https://doi.org/10.1002/adhm.202503487

DOI: 10.1002/adhm.202503487

C. Goldin, S. Esperante, D. Alvarez-Paggi
Centro de Rediseño e Ingeniería de Proteínas (CRIP)
Instituto de Investigaciones Biotecnológicas (IIB)
Universidad Nacional de San Martín (UNSAM)
Buenos Aires B1650, Argentina
E-mail: dalvarezpaggi@iib.unsam.edu.ar

C. Goldin, C. A. Prato, A. L. Paletta, M. V. Tribulatti, S. Esperante, D. Alvarez-Paggi
Consejo Nacional de Investigaciones Científicas y Técnicas
Buenos Aires C1425, Argentina

C. A. Prato, A. L. Paletta, M. V. Tribulatti
Instituto de Investigaciones Biotecnológicas
Escuela de Bio y Nanotecnologías (EByN)
Universidad Nacional de San Martín (UNSAM)
Buenos Aires, Argentina

of mAbs diminished with the emergence of new viral variants, and they suffer from rapid systemic clearance and short lung retention times,[19,20] which may limit the efficacy of such treatments, particularly for local delivery. Additionally, convalescent plasma is only effective at very early stages of infection,[8] requiring high titers that may be difficult to obtain. Prophylactic approaches such as nasal delivery of neutralizing antibodies have shown potential, particularly in high-risk exposure scenarios, but remain cost-prohibitive for large-scale deployment. Furthermore, clinical evidence has shown that effective treatments for COVID-19 require a high density of inhibitory domains to maximize viral neutralization.[21] This created a vacancy that ignited all kinds of efforts in developing new antivirals or repurposing existing drugs, many of which ultimately failed to demonstrate clinical benefit.[22]

Altogether, these challenges underscore the need for cost-effective, scalable, efficient, and easily customizable therapeutic strategies against emerging pathogens with pandemic potential. Nanoparticle-based strategies constitute an attractive alternative to ABTs for virus capture and neutralization, since they exhibit prolonged retention times, high surface area for cargo presentation, high-density clustering of binding domains, and reduced production costs.[17,23,24]

SARS-CoV-2 entry in host cells is mediated by the interaction between the receptor binding domain (RBD) from viral Spike (*S*) glycoprotein and the cell surface angiotensin-converting enzyme 2 receptor (ACE2r) expressed by nasal ciliated cells, alveolar pneumocytes, exocrine pancreas, intestinal tract, seminal vesicle, epididymis, proximal renal tubules, heart muscle and thyroid gland.[25–29] Thus, this interaction has been a primary target for ABTs but also for peptides, small molecules, and DNA aptamers.[30,31] However, except for antibodies, these molecules typically display moderate binding affinity.

An innovative approach to creating SARS-CoV-2 neutralizing molecules developed by Baker's lab involves the AI-assisted design of protein minibinders[21]—small, highly stable all-α domains (**Figure 1A**)—structurally inspired by ACE2r but designed entirely *de novo*. The binding sites of two of these binders, named LCB1 and LCB3, are hidden in the closed *S* conformational state and require at least two open RBDs for trivalent recognition. LCB1 and LCB3 are small three-helix bundles that establish multiple hydrogen bonds and salt bridges with the RBD, resulting in high neutralizing potency, with Half Maximal Inhibitory Concentration (IC_{50}) values ranging from 24 pM to 14 nM depending on the assay. Interestingly, these domains bind to slightly different S pockets and they do it in opposite orientations, such that their N- and C-termini adopt inverted spatial dispositions when complexed with the RBD (Figure 1B).

Despite the high affinity of LCB1 and LCB3, the typically short half-lives of small polypeptides imply that they would benefit from a high molecular weight scaffold to prevent rapid clearance. Additionally, given the trimeric and dynamic nature of S, the high-density display of minibinders on a stable multimeric scaffold could significantly enhance affinity and avidity. Thus, rather than relying solely on AI-derived molecules, we thought of leveraging structural virology principles to rationally design a multivalent scaffold that optimally positions and potentiates the activity of these RBD binders.

We exploited the scaffold properties of nucleoproteins (*NP*) from the Mononegavirales order to engineer high-affinity multivalent neutralizing particles with therapeutic potential. During viral replication, these *NP*s naturally oligomerize into rod-like structures that protect the viral genome. Recombinant expression of *NP* often yields homogeneous monodisperse ring-like particles (RLPs) that self-assemble directly in vivo during expression, prior to protein purification.[32,33] These RLPs have been used as scaffolds to display antigens and other cargoes as fusions at either terminus of the *NP*, without interfering with their ability to oligomerize into well-defined nanostructures.[34–36]

RLPs derived from respiratory syncytial virus (RSV) *NP* form monodisperse, decameric, and highly stable rings, resilient to disassembly[32] and amenable to protein engineering. These RLPs have been exploited as scaffolds to generate particles decorated with 10 identical cargoes.[34] Crucially, both the N- and C-termini of each *NP* subunit extend outward into the solvent from the same face of the ring, creating up to 20 spatially co-localized anchor points for cargo attachment. This intrinsic polarity and local clustering enable precise control over cargo density and spatial orientation, optimizing avidity and multivalent engagement of oligomeric viral targets when incorporating binders. Thus, we exploited the combination of i) the availability of both of N- and C- termini in the RLP scaffold and ii) minibinders with opposite orientation vectors (Figure 1) to rationally design RLPs of defined size that present binders in an optimal functional orientation for *S* binding. RLP-minibinders coupling yields homogeneous, monodisperse RLPs with a high density of binder domains (20 per macromolecule). These multivalent and high-density decorated nanostructures neutralized the fusion of SARS-CoV-2 pseudotyped virus-like particles (SC2-VLPs) to the membrane of ACE2r-expressing human cells with half-maximal inhibitory concentration (IC_{50}) values in the fM range. Moreover, they also neutralized both the ancestral Wuhan and Omicron BA.5 strains with up to 5-fold increased potency compared to a passive heterologous immunotherapy in Phase 2/3 clinical trials.[13]

Our RLP binders are biocompatible, soluble, stable, effective, and easily produced and purified. In addition, they can also be integrated into ELISA *S* detection platforms to enhance sensitivity at an affordable cost. By combining therapeutic, prophylactic, and diagnostic functionalities within a single protein-only

O. Bárcenas
Institute for Advanced Chemistry of Catalonia (IQAC) of the Spanish Council for Scientific Research (CSIC)
Barcelona, Spain

D. H. Murgida
Departamento de Química Inorgánica
Analítica y Química Física
Facultad de Ciencias Exactas y Naturales
Universidad de Buenos Aires
Buenos Aires C1428, Argentina

D. H. Murgida
Instituto de Química Física de los Materiales
Medio Ambiente y Energía (INQUIMAE)
CONICET-UBA
Buenos Aires C1428, Argentina

S. Ventura
Hospital Universitari Parc Taulí
Institut d'Investigació i Innovació Parc Taulí (I3PT-CERCA)
Universitat Autònoma de Barcelona
Sabadell 08208, Spain

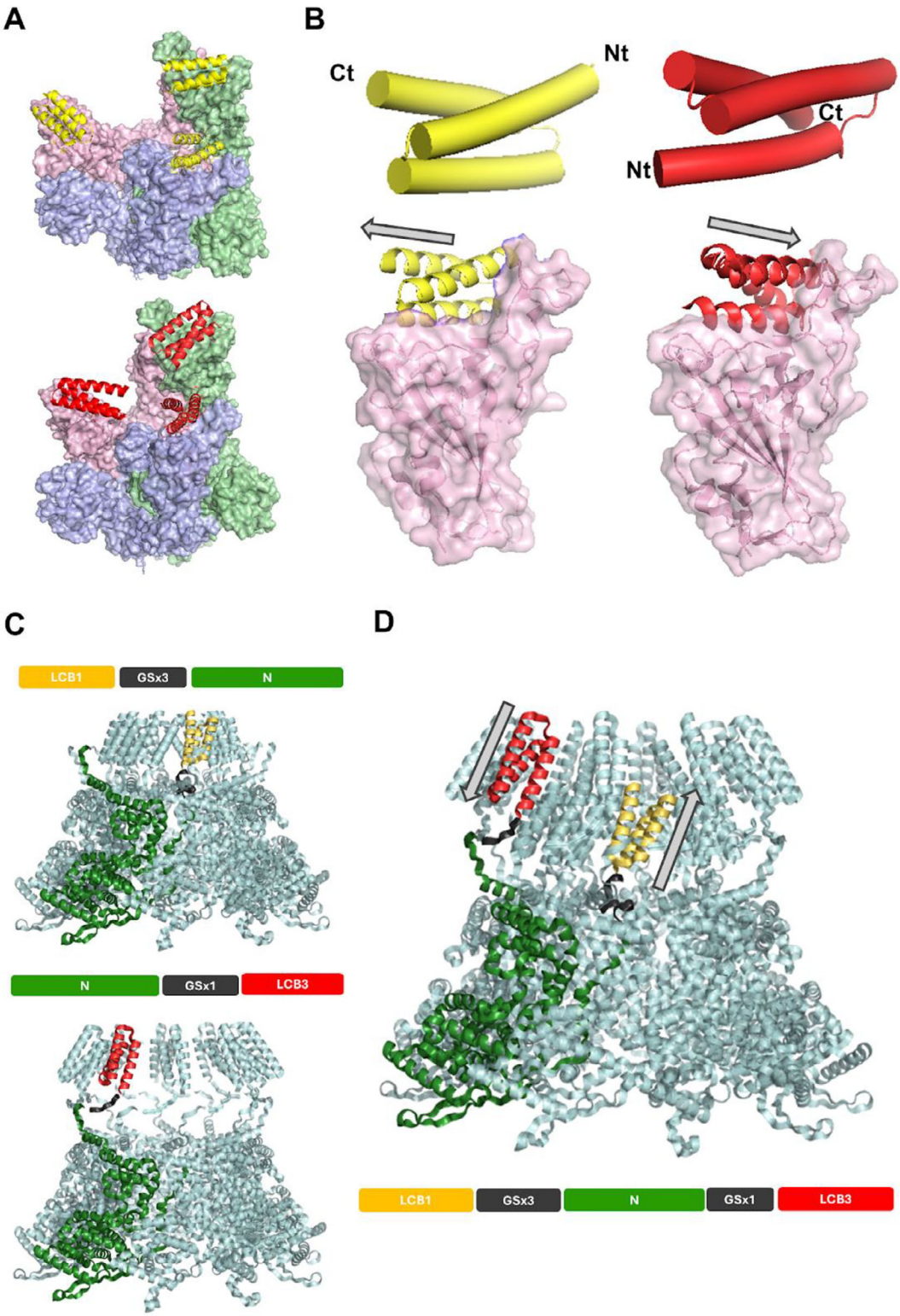

Figure 1. Rational design and structural modeling of RLPs fused to SARS-CoV-2 minibinders. A) Structural analysis of LCB1 (yellow, PDB ID 7JZL) and LCB3 (red, PDB ID 7JZN) in complex with the SARS-CoV-2 Spike. B) Both LCB1 and LCB3 are small three-helix bundles with different up–down–up (LCB1, PDB ID 7JZU) or down–up–down (LCB3, PDB ID 7JZM) arrangements, which define their binding polarity. Gray arrows indicate the orientation of each minibinder. C) Computational models of the single-fusion constructs. RLP-1 (top) carries LCB1 fused to the N-terminus of RLP via a 3× Gly/Ser linker, and RLP-3 (bottom) carries LCB3 fused to the C-terminus of NP via a 1× Gly/Ser linker. D) Computational model of the dual-fusion construct RLP-1,3, in which LCB1 and LCB3 are simultaneously attached to the N- and C-termini of NP, respectively.

system, they offer a versatile and cost-effective alternative to ABTs.

This work exemplifies the convergence of AI-enabled molecular design with classical structure-based engineering, enabling the creation of next-generation bio-nanomaterials with synergistic properties. Our platform showcases the ability to generate customizable multivalent binders with exceptional neutralizing capacity, applicable to a broad range of diseases where ABTs remain only partially effective, or where rapid and scalable responses to emerging pathogens are urgently required.

2. Results and Discussion

2.1. Design, Conformational Characterization, and Stability RLP-LCB Proteins

We analyzed the structure of the RSV *NP* RLP (RLP) (PDB ID 2WJ8)[37] and of the LCB1 (PDB ID 7JZU) and LCB3 (PDB ID 7JZM) minibinders in the context of their complex with RBD (Figure 1A). These minibinders were *de novo* designed to tightly bind to SARS-CoV-2-*S*-RBD.[21,38] Although they engage overlapping, yet not identical, binding interfaces (Table S1, Supporting Information), their structural orientation within each differs. Both LCB1 and LCB3 are small 3-helix bundles, but whereas LCB1 (PDB ID 7JZL) binds in an up-down-up orientation, LCB3 (PDB ID 7JZN) does so in a down-up-down conformation. This defines an overall polarity for each minibinder, where they bind in distinct, antiparallel symmetries in terms of their N-C termini orientation (Figure 1B).

We leveraged the availability of both the N- and C-terminal ends of the *NP* RLPs to rationally design fusion constructs that preserve the functional orientation of each minibinder. In this way, LCB1 was fused to the N-terminus and LCB3 to the C-terminus of *NP*, thus preserving their antiparallel symmetry for complex formation with RBD. Although both termini emerge from the same side of the RLPs, the N- and C-termini of RSV *NP* are not equally solvent exposed. Therefore, we used different linker lengths to ensure that both minibinders were well-displayed for target binding. Linkers were modeled using full-atom and coarse-grained targeted molecular dynamics (TMD) simulations, in combination with rigid body modeling. A 3X Gly/Ser linker for LCB1 and a 1X Gly/Ser linker for LCB3 proved sufficient to grant both minibinders with solvent accessibility in their correct functional orientations (Figure 1C,D).

We generated three fusion proteins, LCB1 fused to the N-terminus of *NP*, LCB3 fused to the C-terminus of *NP*, and a double fusion of LCB1 and LCB3 to the N- and C-termini, respectively. They were all designed to form decameric RLPs labeled RLP-1, RLP-3 and RLP-1,3, respectively (Figure 1C,D). Coarse-grained molecular dynamics of the largest RLP-1,3 fusion indicated that the two binding moieties remain accessible, without any steric hindrance between the 10 outer and 10 inner LCB subunits. LCB1, fused at the N-terminus, is more rigid and closely packed in the scaffold, whereas LCB3, populating the external corona, is more mobile and can diffuse farther from the scaffold's center (Figure S1, Supporting Information).

The three fusion proteins, along with a control RLP lacking any fused cargo, were recombinantly expressed and purified (See Methods and Figure S2, Supporting Information), with yields of 38, 37, 23, and 12 mg L^{-1} for RLP, RLP-1, RLP-3, and RLP-1,3, respectively. All fusions exhibited well-defined secondary structures. Far-UV circular dichroism (CD) showed spectra dominated by strong α-helical signals, with characteristic minima at 208 and 222 nm, consistent with the expected helical content of both the RLP scaffold and the fused minibinders[21,32] (**Figure 2**).

The quaternary structure of the resulting protein assemblies was evaluated by transmission electron microscopy (TEM) (**Figure 3**). All constructs formed discrete, ring-shaped nanoparticles with diameters between 14 and 16 nm, depending on the specific fusion design, consistent with the previously described RLP decamers[32] indicating that incorporation of the minibinders does not impair the ability of the proteins to self-assemble into defined, symmetric particles (Figure 3; Tables S2 and S3, Supporting Information). The preservation of this architecture further implies that each protomer is correctly folded, allowing productive inter-subunit interactions.

The homogeneity and size distribution of the RLPs were analyzed by dynamic light scattering (DLS) (Figure 3). Monodisperse populations with average hydrodynamic diameters ≈ 20 nm and low polydispersity indices (0.1-0.4) were observed (Table S2, Supporting Information), in agreement with TEM data. No signs of aggregation or multimodal populations were detected, highlighting the uniformity of the samples.

TEM imaging performed after one month of storage at 4 °C revealed no detectable changes in morphology or size distribution. The particles retained their original oligomeric state and ring-like morphology. DLS analysis during the same period corroborated these findings, revealing consistent size distributions and correlation profiles, with only small subpopulations of higher-order assemblies appearing at later incubation times, further underscoring the particles' structural robustness under standard storage conditions (Figure S3; Table S2, Supporting Information).

2.2. RLPs Effectively Compete with the Spike RBD-ACE2 receptor Interaction

We assessed the capacity of the engineered RLP constructs to interfere with the interaction between the RBD of SARS-CoV-2 and the human ACE2 receptor (ACE2r). To this end, we employed a competition-based Lumit immunoassay, where inhibition of RBD–ACE2r binding results in a measurable decrease in luminescence. Serial dilutions of RLP, RLP-1, RLP-3, and RLP-1,3 were incubated with SARS-CoV-2 RBD-rabbit Fc (rFc-RBD) and human ACE2r-mouse Fc (mFc-ACE2). The interaction was quantified using a split-luciferase system consisting of an anti-mouse Ab-LgBiT and anti-rabbit Ab-SmBiT. Luminescence served as a direct readout of the RBD–ACE2r binding strength.

All three engineered RLPs potently decreased luminescence in a concentration-dependent manner. RLP-1, RLP-3, and RLP-1,3 showed IC_{50} values of 48.6, 30.3, and 57.7 pM, respectively (**Figure 4**). These values are better than the ones recorded with the same assay for four different investigational anti-SARS-CoV-2 Spike RBD antibodies of chimeric mouse/human (Sino Biological 40150-D001 and 40150-D002) and human origin (Active Motif 91361 and Biolegend 938502), which exhibited IC_{50} values of 1870, 250, 430, and 370 pM; respectively.[39] Of note, control RLP exhibited negligible inhibition, confirming the specificity of the

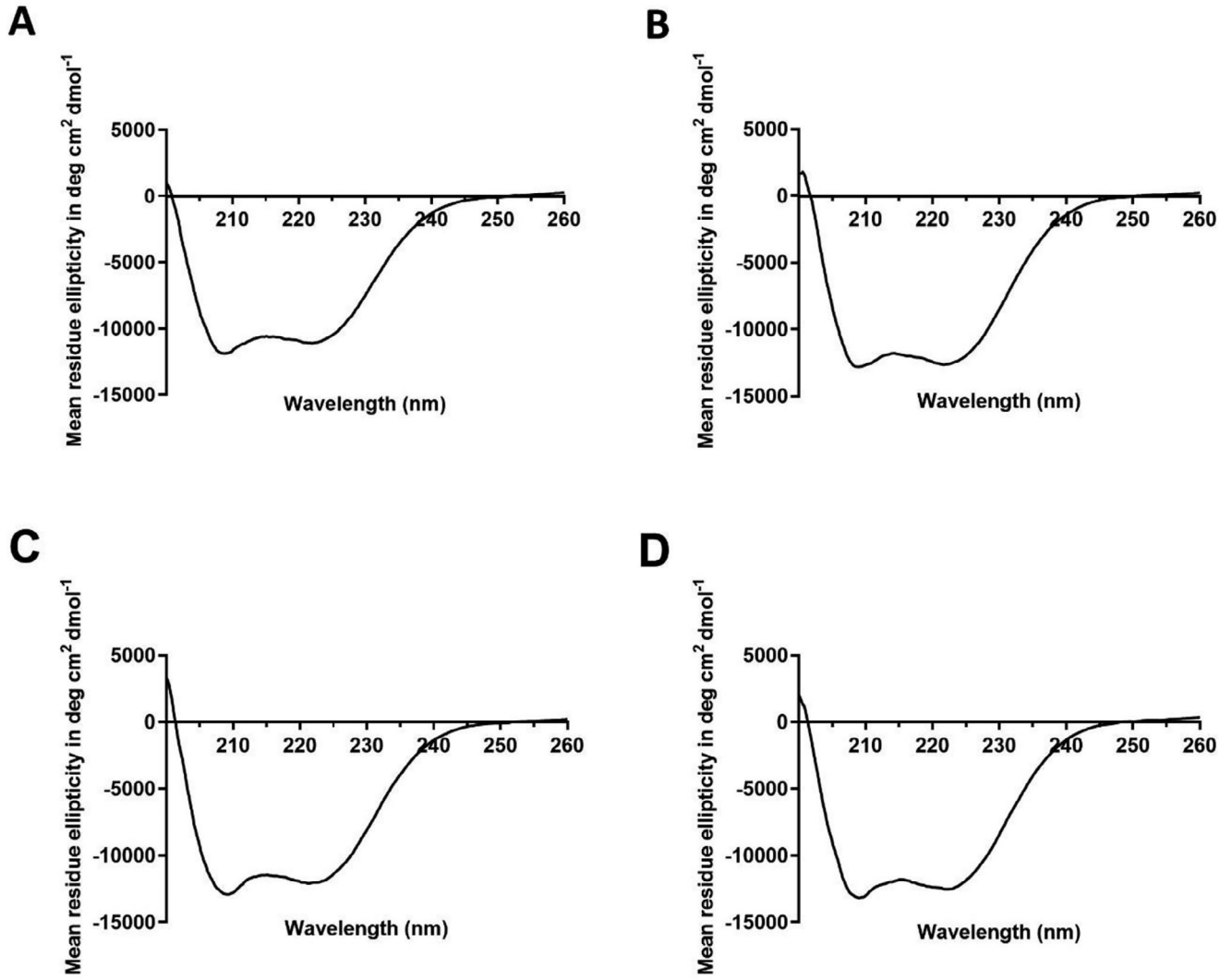

Figure 2. Secondary structure of soluble RLP nanoparticles analyzed by circular dichroism (CD) spectroscopy. Spectra were recorded from 260 to 200 nm in 20 mM sodium phosphate buffer (pH 8.0) containing 0.15 M NaCl. A) RLP; B) RLP-1,3; C) RLP-1; D) RLP-3. All RLPs spectra present a major contribution of α-helical signals, compatible with RLPs and minibinders structures.

observed effects. Nonlinear regression showed a slight leftward shift for RLP-3 relative to RLP-1 and RLP-1,3, consistent with a modestly lower IC_{50}. Pairwise comparisons indicated this difference is significant versus RLP-1 (P = 0.028) and RLP-1,3 (P = 0.004), whereas the difference between RLP-1 and RLP-1,3 is not significant (P = 0.549).

2.3. RLP-Binders Block Viral Entry

In a similar manner to neutralizing antibodies, molecules that bind the *S* glycoprotein on the viral surface with high affinity may prevent viral entry into the host cell, thereby offering protection against infections or sequestering residual viral particles that may persist in individuals with long COVID. Therefore, we investigated the ability of the RLPs to block RBD-ACE2 binding and the subsequent membrane fusion event, in the context of full viral particles.

To do so, we used a HiBiT-based bioluminescence assay, a well-validated technology for SARS-CoV-2 investigation,[24,40,41] which utilizes SARS-CoV-2 pseudotyped virus-like particles (SC2-VLPs)[42] (See Methods section). In this system, successful fusion of SC2-VLPs with ACE2-expressing cells leads to the internalization of HiBiT and its complementation with intracellular LgBiT, restoring luminescence. Neutralizing molecules that inhibit SC2-VLPs' entry prevent this complementation, resulting in a decrease in luminescence (**Figure 5**).

To evaluate the neutralizing potency of our nanoparticles, SARS-CoV-2 *S* (G614) HiBiT- pseudotype VLPs were incubated with RLP-1, RLP-3, and RLP-1,3 in a range of 4000-0.004 pM, and then added to the hACE2-HEK293T (LgBiT) target cells, and the neutralizing IC_{50} values were determined (Figure 5). The neutralization IC_{50} values for RLP-1, RLP-3, and RLP-1,3 were 16.07, 16.76, and 0.57 pM, respectively. Pairwise analyses indicated that RLP-1,3 neutralized significantly more potently than both RLP-1 (p = 0.014) and RLP-3 (p = 0.029), while no

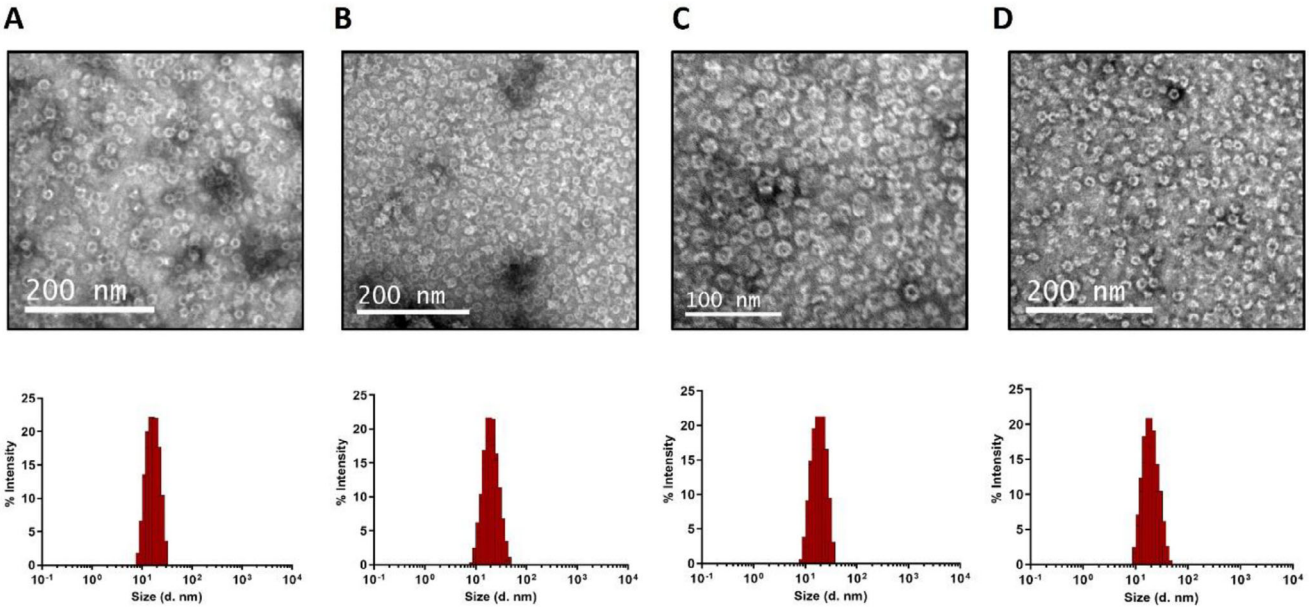

Figure 3. Morphological characterization and size distribution of the RLPs. A) RLP; B) RLP-1,3; C) RLP-1; D) RLP-3. For each sample, the top panel shows transmission electron micrographs (TEM) of negatively stained nanoparticles, and the bottom panel presents the corresponding size distribution determined by dynamic light scattering (DLS).

significant difference was observed between RLP-1 and RLP-3 ($p = 0.927$).

The RLP-1 and RLP-3 IC_{50} values exhibit a substantial improvement over benchmark mAbs, such as Bamlanivimab,[43] Imdevimab,[44] or Etesevimab,[45] that target *S* and are being used individually or in combination against COVID-19,[46] as well as over multimeric scaffolds incorporating multivalent minibinders.[47] All these constructs were tested using the same HiBiT assay (**Table 1**). The exceptional performance of RLP-1,3 cannot be attributed solely to the increased number of binding sites. Instead, it reveals a striking synergistic effect between LCB1 and LCB3 minibinders, likely resulting from cooperative interactions that enhance binding avidity and efficiency, which translates into IC_{50} values 500–1000 times lower than those of state-of-the-art mAbs, whether measured by molar concentration or mass (Table 1). Based on our TMDs (Figure S1, Supporting Information), we hypothesized that the synergistic effect of both binders, beyond providing avidity by displaying multiple binding sites, could likely explained by LCB3 being the leading player in the initial stages of the virus capture mechanism, while LCB1 can anchor the interaction more solidly.

2.4. Virus Neutralization

After validating the RLPs with the HiBiT assay, we next evaluated their neutralizing potency against authentic SARS-CoV-2, using viral neutralization assays with both the Wuhan strain and the Omicron BA.5 variant (**Figure 6**). Serial dilutions of each RLP were incubated with either strain of SARS-CoV-2 at 37 °C for an hour and then added to Vero cells monolayers for an additional hour at the same temperature (multiplicity of infection, MOI = 0.004). The viral neutralization titer was quantified by monitoring the cytopathic effect (CPE), measuring media absorbance at 585 nm, and applying non-linear curve fitting for IC_{50} determination (see Methods). As a positive control, we determined the neutralizing potency of a hyperimmune equine sera (HES), a clinically approved immunotherapy developed by Inmunova and commercially available as CoviFab, under the same experimental conditions.[47] In the case of the Wuhan strain, all RLPs outperform the HES, with RLP-1,3 showing a tenfold increase in potency, which is consistent with the synergy observed in the HiBiT assay (**Table 2**).

As expected, when tested against the Omicron BA.5 variant, all samples (RLPs and HES) showed a reduction in potency, reflecting the immune evasion properties of this variant. RLP-3 is particularly affected, aligning well with previous reports,[48] likely due to the accumulation of escape variants that impact the LCB3-RBD interface as the minibinders were designed based on the Wuhan RBD-ACE2 interaction. This translates to RLP-1 and RLP-1,3 exhibiting similar curves, showing no synergistic interaction between LCB1 and LCB3 for this viral variant. However, it must be emphasized that the neutralizing power of RLP-1 and RLP-1,3 against Omicron BA.5 is still greater than HES's potency against the original Wuhan strain.

These results highlight that i) the highly ordered, topologically oriented minibinders anchored on the RLP scaffold can exert a neutralizing effect that surpasses antibody-based therapeutics (ABTs), such as mAbs and HES, ii) the combination of different binders within the same scaffold results in a synergistic effect against viral variants for which both binders are functional, and iii) the design offers built-in functional redundancy; Even if any of the binders fail to neutralize emerging variants, the remaining binder(s) can rescue the neutralization function, underscoring the potential of these modular, multi-component scaffolds as a versatile strategy to counteract evolving viral threats.

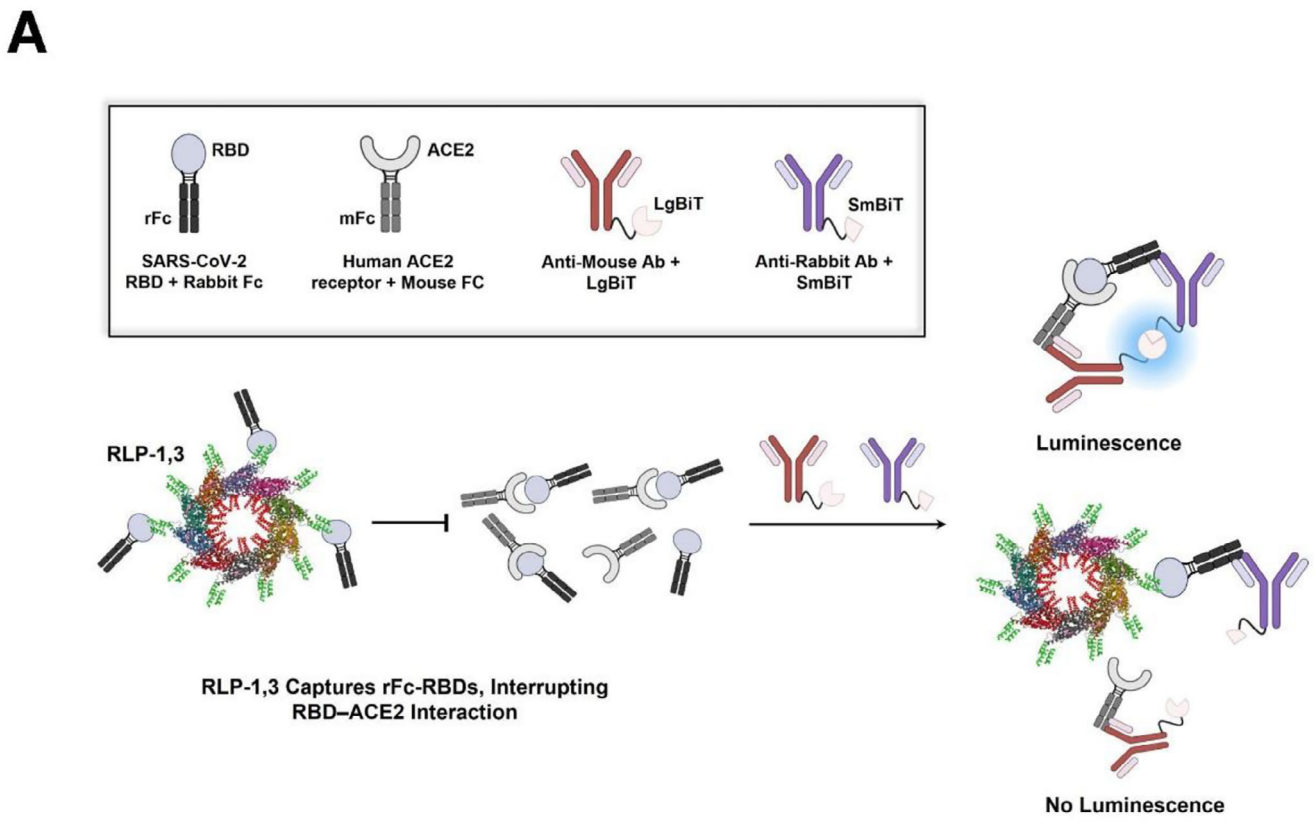

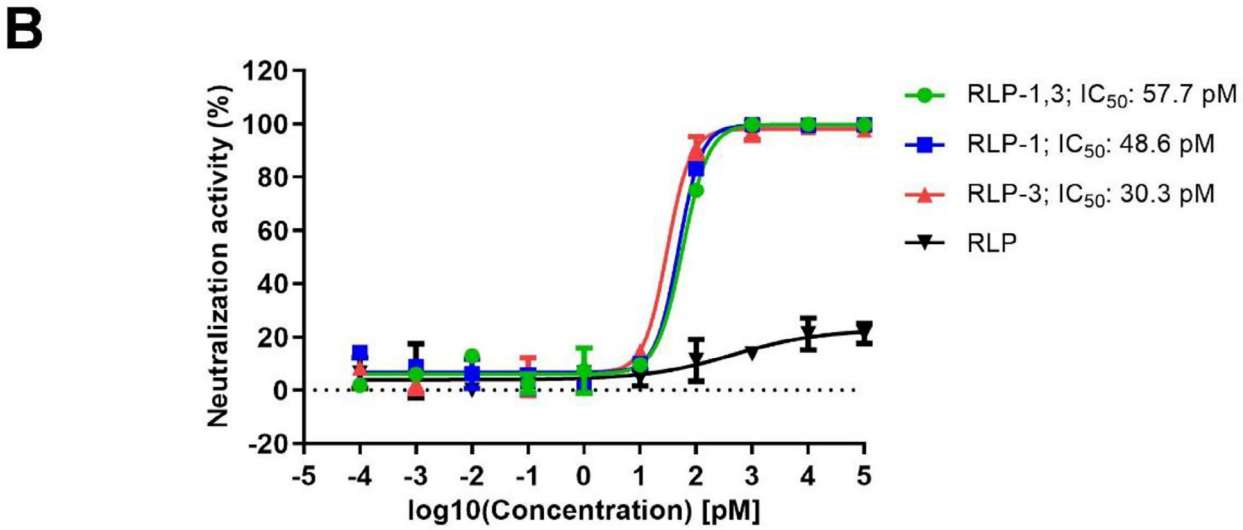

Figure 4. Inhibition of the RBD-ACE2 interaction by RLPs using the Lumit SARS-CoV-2 spike RBD, ACE2r immunoassay. A) Schematic representation of the Lumit™ SARS-CoV-2 Spike RBD–ACE2 immunoassay. Created with BioRender.com. B) Results represent the mean values of two technical replicates ± SD. IC_{50} values were determined by nonlinear regression using a four-parameter logistic model.

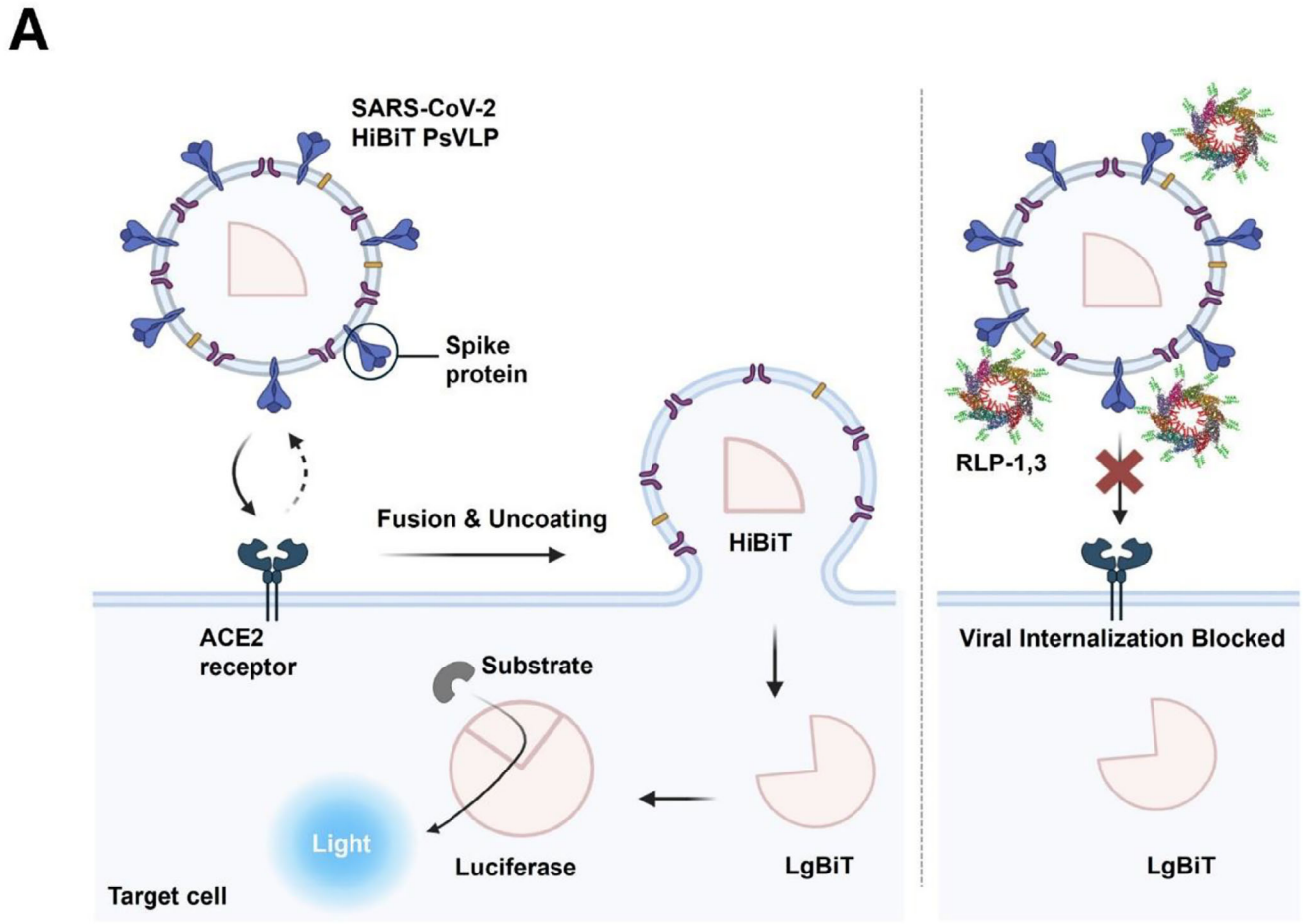

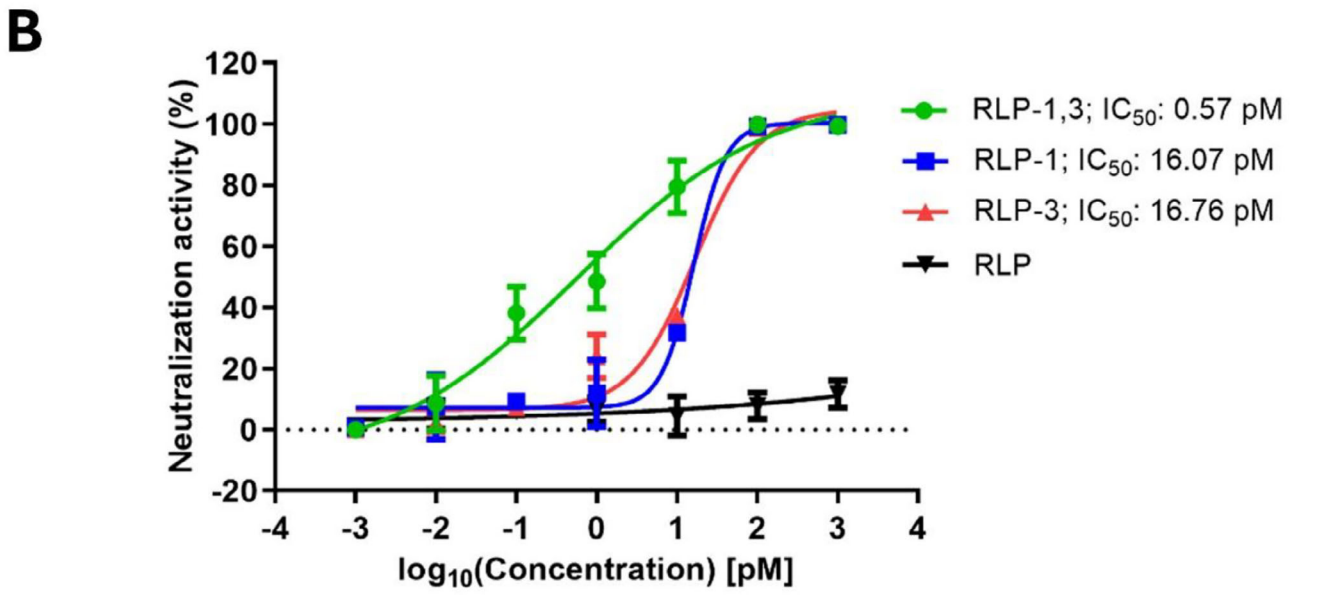

Figure 5. Neutralization effect of RLPs against SARS-CoV-2 virus using the SARS-CoV-2 HiBiT-pseudotype VLP-based assay. A) Schematic representation of the SARS-CoV-2 HiBiT-pseudotype VLP cellular assay based on NanoBiT technology (Promega). Created with BioRender.com. B) Results represent the mean values of two technical replicates ± SD. Data were fitted with a four-parameter logistic model to determine IC_{50}.

Table 1. SARS-CoV-2 HiBiT-pseudotype VLP-based assay response to neutralizing antibodies minibinder-coupled oligomeric scaffolds.

Anti-SARS-CoV-2 Spike mAb/binder	IC_{50} [ng/mL]	IC_{50} [pM]
Bamlanivimab[a)]	34	232.9
Imdevimab[a)]	72	499.5
Etesevimab[a)]	230	1629.1
OligoBinder-1[24]	88.2	120.7
OligoBinder-3[24]	101.1	127.8
RLP-1	8.62	16.07
RLP-3	9.53	16.76
RLP-1,3	0.35	0.57

[a)] Data as provided by Promega Biotech Ibérica, S.L.

2.5. RLP Nanoparticles Are Biocompatible and Stable in Human Plasma

Every nanomaterial intended for biomedical use should be biocompatible. As a proof-of-concept of our constructs' safety, we determined the metabolic activity of human cells exposed to the RLPs. HeLa cells were treated with increasing concentrations of each purified RLP (1 to 10 μM) and incubated for 72 h. Cell viability was measured using the PrestoBlue assay, a resazurin-based reagent that fluoresces in proportion to cellular metabolic activity. For all concentrations of the RLP constructs, cell viability remained identical to the control group, indicative of the RLPs' biocompatibility (**Figure** 7A).

The bioavailability of active protein-based materials is critical for their biomedical applications, as polypeptides are inherently susceptible to plasma proteolytic enzymes. Therefore, we investigated the stability of the RLP constructs upon incubation in human plasma for 48 h at 37 °C by assessing protein integrity using western blot (Figure 7B). RLPs in plasma at time zero were used as positive control. As shown in Figure 7, all RLP constructs remained stable for 48 h in plasma, with no detectable degradation. Considering the remarkable stability of the RLPs quaternary structure that cannot be disrupted even in the presence of high concentrations of denaturing agents,[32] the stable, non-cleaved proteins, are expected to remain in their oligomeric state.

2.6. RLPs Can Be Used for Antigen Detection

In addition to their therapeutic potential, RLPs may also serve as effective tools for antigen detection, offering an alternative to conventional ABTs. To explore this diagnostic capability, we developed a sensitive enzyme-linked immunosorbent assay (ELISA) using the dual-minibinder construct, RLP-1,3, for detecting the SARS-CoV-2 *S* protein. This assay incorporates a signal amplification strategy that leverages both the multimeric and multivalent nature of the RLP scaffold. In this assay, the detection antibody specifically binds to the RLP rather than the antigen, enhancing sensitivity. The principles of the assay are schematically shown in **Figure** 8A. Plate wells were coated with horse anti-*S* $F(ab')_2$, followed by incubation with serial dilutions of recombinant *S* protein. RLP-1,3 was then added to bind the immobilized antigen, and detection was completed using a mouse anti-*NP* antibody, followed by an HRP-conjugated anti-mouse secondary antibody. This modified ELISA detects concentrations of SARS-CoV-2 Spike protein in solution as low as 9 ng mL^{-1} (Figure 8B), offering superior sensitivity compared to available commercial kits with a limit of detection of 60 ng mL^{-1}.[49]

3. Conclusion

This work presents a robust, scalable, and modular strategy for generating multivalent, protein-only nanoparticles that can replace or complement conventional antibody-based approaches for both therapeutic and diagnostic applications. These molecules are the result of rationally interphasing previously AI-designed minibinders with a logically selected scaffold, to produce soluble, properly folded, and assembled RLPs that are homogeneous, monodisperse, biocompatible, and highly stable, all while maintaining low production complexity and costs, comparing favorably to mAbs and other biologics (**Table** 3).

The multimeric display of binders with complementary geometries (LCB1 and LCB3) on a polarized scaffold facilitates high-density clustering of binding domains in a functionally oriented configuration. This arrangement enhances avidity and target engagement while also producing synergistic effects that lead to ultrapotent viral neutralization in the fM range in the VLP-based assay, surpassing the performance of individual binders and even clinically used neutralizing antibodies reported under comparable conditions.[39] Furthermore, by combining multiple binders targeting partially overlapping epitopes, RLPs offer the ability to compensate for loss of activity due to viral escape mutations, which is critical for addressing rapidly evolving pathogens. Overall, we present a pathogen-agnostic scaffold that is rationally designed to accommodate virtually any protein—or a combination of two—whether naturally occurring, rationally engineered, or AI-designed, in an optimal topology for display and function. The versatility of this system allows for the exploration of additional configurations by incorporating alternative binders, tuning linker length and flexibility/rigidity, and employing different tethering strategies, which will be the focus of future studies.

Beyond its therapeutic potential, the versatility of the RLP platform was demonstrated by its successful implementation in an amplified ELISA format for Spike detection, capable of enhancing sensitivity in a cost-effective manner. These findings exemplify the power of integrating AI-driven molecular design with classical structure-based protein engineering to create next-generation bio-nanomaterials with properties that would be unattainable through either strategy alone.

In the face of continuing viral evolution and the inevitability of future pandemics, the need for rapid, adaptable and affordable biomedical solutions is more urgent than ever. The RLP-minibinder system provides a generalizable and scalable modular plug-and-(dis)play framework for targeting a broad spectrum of pathogens, representing a promising alternative to conventional ABTs, since it combines diagnostic and therapeutic potential in a single, compact, and customizable protein architecture.

4. Experimental Section

Protein Design, Expression and Purification: The RLP designs were built by manually threading flexible linkers to connect models of folded do-

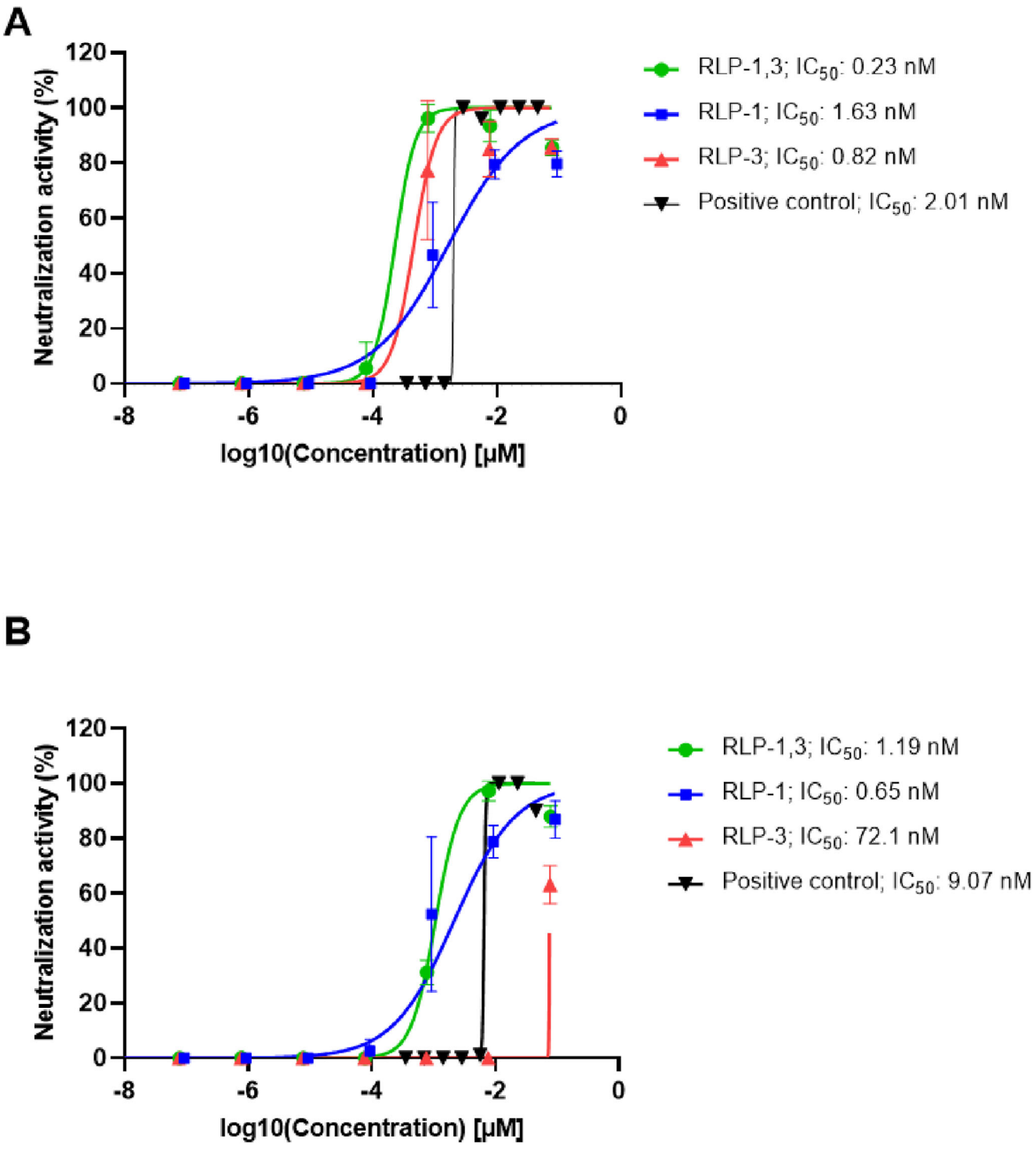

Figure 6. Evaluation of the neutralizing potency of RLPs against Wuhan and Omicron BA.5 strains of SARS-CoV-2. A,B) Neutralization activity of RLP-1, RLP-1.3, and RLP-3 against (A) Wuhan and (B) Omicron BA.5 SARS-CoV-2 strains. Dose-response curves represent the mean ± SD of three replicates. IC_{50} values were determined by nonlinear regression using a variable slope model.

Table 2. Neutralizing activity of the RLPs against the Wuhan and Omicron BA.5 strains of SARS-CoV-2.

Neutralizing Agent	IC_{50} [Wuhan Strain, nM]	IC_{50} [BA.5 Variant, nM]
HES[a)]	2.01	9.07
RLP-1	1.63	0.65
RLP-3	0.82	72.1
RLP-1,3	0.23	1.19

[a)] HES (hyperimmune equine serum), a clinically approved therapy, was included as a positive control.

mains, predicted with AlphaFold 2 V1.5.5 and assembled via homology modeling to existing structures of RSV ring-like particles.

The DNA sequences encoding for optimized LCB1 and LCB3 proteins[38] were subcloned into a pET-30 vector (GenScript), containing the RSV *NP* coding sequence with an N-terminal 6xHis tag (see sequence design in Figure 1). The RSV NP gene was likewise expressed from the pET-30 vector to serve as a control. The DNA sequences of the optimized versions of LCB1 and LCB3 were selected for their improved thermal stability, high expression in *E.coli*, and enhanced compatibility with multivalent designs to enable stronger and more durable binding to *S*.[21,38] The plasmids were transformed into *E. coli* BL21 (DE3) strain. Then, the transformed cells were grown overnight in LB medium containing 50 μg mL^{-1} kanamycin at 37 °C with agitation. Subsequently, overnight cultures were diluted 1:100 in fresh LB medium supplemented with 50 μg mL^{-1} kanamycin and incubated at 37 °C with agitation to reach an optical density (600 nm) of 0.4. To induce protein expression, 0.4 mM IPTG was added, and cultures were incubated at 20 °C for 16 h with agitation. Samples from non-induced and induced cultures were taken to analyze soluble and insoluble fractions using 15% SDS-PAGE. Cells from a 1 L culture were harvested by centrifugation at 6000 rpm for 30 min at 4 °C. Collected cell pellet was resuspended in lysis buffer (20 mM sodium phosphate pH 8.0, 200 mM NaCl), and lysed by sonication on ice for 15 min (2 s on / 3 s off, 40% amplitude). Lysates were centrifuged at 20000 rpm for 30 min at 4 °C to obtain clarified supernatants containing the soluble protein fraction, which was subsequently enriched for the protein of interest by precipitation with 55% ammonium sulfate for 2 h at 4 °C under gentle agitation. Following precipitation, the protein was pelleted by centrifugation at 12 000 rpm for 15 min at 4 °C, resuspended in dialysis buffer (20 mM sodium phosphate pH 8.0, 500 mM NaCl), and dialyzed overnight at 4 °C to remove residual ammonium sulfate. The sample was then filtered through a 0.45 μm filter and loaded onto a pre-equilibrated HisTrap FF crude column for His-tag affinity purification. The column was washed with buffer (20 mM sodium phosphate pH 8.0, 500 mM NaCl, 20 mM imidazole) and eluted with buffer containing 500 mM imidazole (20 mM sodium phosphate pH 8.0, 500 mM NaCl, 500 mM imidazole). Eluted samples were dialyzed overnight at 4 °C in buffer containing 20 mM sodium phosphate (pH 8.0) and 150 mM NaCl, then filtered through a 0.2 μm filter and loaded onto a pre-equilibrated HiLoad 16/600 Superose 6 prep grade (pg) column using the same buffer. Fractions with 100% homogeneity of purified RLPs were selected based on dynamic light scattering (DLS), and their purity was confirmed with a 15% SDS-PAGE gel. Protein quantification was performed by absorbance using (Equation 1), which allows the separation of protein and RNA contributions. Fractions containing purified proteins were snap-frozen in liquid nitrogen and stored at −80 °C.

$$[Protein] = \frac{\left[A_{260} - \left(\frac{\varepsilon RNA260}{\varepsilon RNA280}\right) A_{280}\right]}{\left(\varepsilon protein260 - \left(\frac{\varepsilon RNA260}{\varepsilon RNA280}\right) \varepsilon protein280\right) L} \quad (1)$$

where A is absorbance at the specified wavelength, ϵ is the molar extinction coefficient, and L is the absorbance path length.[55]

Circular Dichroism (CD) Spectroscopy: Far-UV CD spectra were acquired in the range of 200–260 nm with a data pitch of 0.2 nm and a bandwidth of 1 nm, at 20 °C, using the Jasco J-815 CD spectropolarimeter (Jasco Corporation, Japan). Each spectrum was an average of 20 accumulations at a scan speed of 100 nm min^{-1} to improve the signal-to-noise ratio. A 0.1 cm pathlength quartz cuvette was filled with the RLP nanoparticles to achieve a final concentration of 10 μM in 20 mM sodium phosphate buffer (pH 8.0) containing 150 mM NaCl.

Dynamic Light Scattering (DLS): DLS measurements were conducted using a Zetasizer Nano-S90 (Malvern Instruments, UK). Sample measurements were acquired from an average of 30 consecutive runs repeated 5 times for each sample. Raw autocorrelation functions were collected using the built-in Zetasizer Software (version 7.11) and exported without further processing. To assess the stability of the RLP nanoparticles during long-term storage at 4 °C, measurements were repeated on days 5, 13, 23, and 30 to evaluate the consistency of the resulting size distributions.

Transmission Electron Microscopy (TEM): To obtain TEM images, 10 μL of the RLP sample (1 μg) were deposited onto the carbon-coated copper grid for 10 min. Grids with adhered nanoparticles were negatively stained with 10 μL of uranyl acetate solution (2% w/v). Excess stain was removed by gently blotting the grid with filter paper strips after 1 min of staining. Resulting grids were visualized using a Hitachi H-7000 transmission electron microscope (Hitachi Ltd., Tokyo, Japan) operated at 125 kV, and images were acquired using a Gatan Erlangshen ES500W CCD camera. Size measurements were performed using ImageJ software (version 1.53e; National Institutes of Health, Bethesda, MD, USA), averaging 100 individual measurements for each RLP nanoparticle.

Interference of the ACE2-RBD Interaction: Lumit SARS-CoV-2 Spike RBD, human ACE2 (hACE2) Immunoassay (Promega Biotech) has been utilized to explore the inhibitory potential of RLPs on the ACE2-RBD interaction. This assay hinges on the interaction of two nonfunctional bits, LgBiT and SmBiT, constituting the full-length functional NanoBiT reporter protein. Serially diluted anti-SARS-CoV-2 RBD RLPs were incubated with RBD-FC (Rabbit Fc) for 30 min. Subsequently, hACE2-FC (Mouse Fc) and Lumit Antibody Mix were introduced. Following a 1-h incubation at room temperature (RT), Lumit detection reagent was applied, followed by an additional 30-min incubation at RT. Luminescence was recorded using the Tecan Spark microplate reader. To eliminate background signal contribution, the light signal from the buffer alone was subtracted from all sample signals. Lumit reagent buffers, containing all assay components except RLPs, were utilized to establish the highest light signal, serving as a reference for calculating signal folds. All luminescence values were expressed as a percentage of ACE2-RBD protein–protein interaction (PPI) activity. Sample % neutralization was calculated by subtracting % PPI activity from 100. Final values represented the mean of two replicates. IC_{50} values were determined using GraphPad Prism V6.01 (GraphPad Software, Inc., USA), employing a non-linear regression (least squares) fitting method.

SARS-CoV-2 Cell Entry Inhibition: To examine the capacity of the RLPs to prevent infection by SARS-CoV-2, we employed a cell-based screening assay using HiBiT-tagged pseudotype VLPs from Promega Biotech. HiBiT technology provides the benefits of high sensitivity and convenience of a single-reagent-addition step, all while overcoming the disadvantage of difficulty quantifying pseudotyped VLP cell entry and membrane fusion. Serial dilutions of the different RLP samples were prepared at a range of 0.004-4000 pM. Next, these 4x RLP dilutions were incubated with HiBiT-tagged SARS-CoV-2 *S* (G614) VLPs (HiBiT-SC2-VLPs) diluted in assay buffer for 30 min at 37 °C.

Next, SARS-CoV-2 HEK293T (LgBiT) target cells were thawed and transferred to a 96 well plate, containing HiBiT-SC2-VLPs and RLPs. After 3 h of incubation at 37 °C, 25 μL of 5x Nano-Glo Live Cell Reagent was added to each well, and luminescence was measured after a 15-min incubation at 37 °C using the Tecan Spark microplate reader.

In the presence of inhibitory particles, SC2-VLPs entry and fusion with target cells were blocked, thereby preventing HiBiT release and resulting in a decrease in the luminescent signal proportional to the concentration of RLP nanoparticles. Baseline signals were established using assay buffer and maximum HiBiT-SC2-VLPs entry into cells was calculated by normalizing the luminescence values (obtained by subtracting the

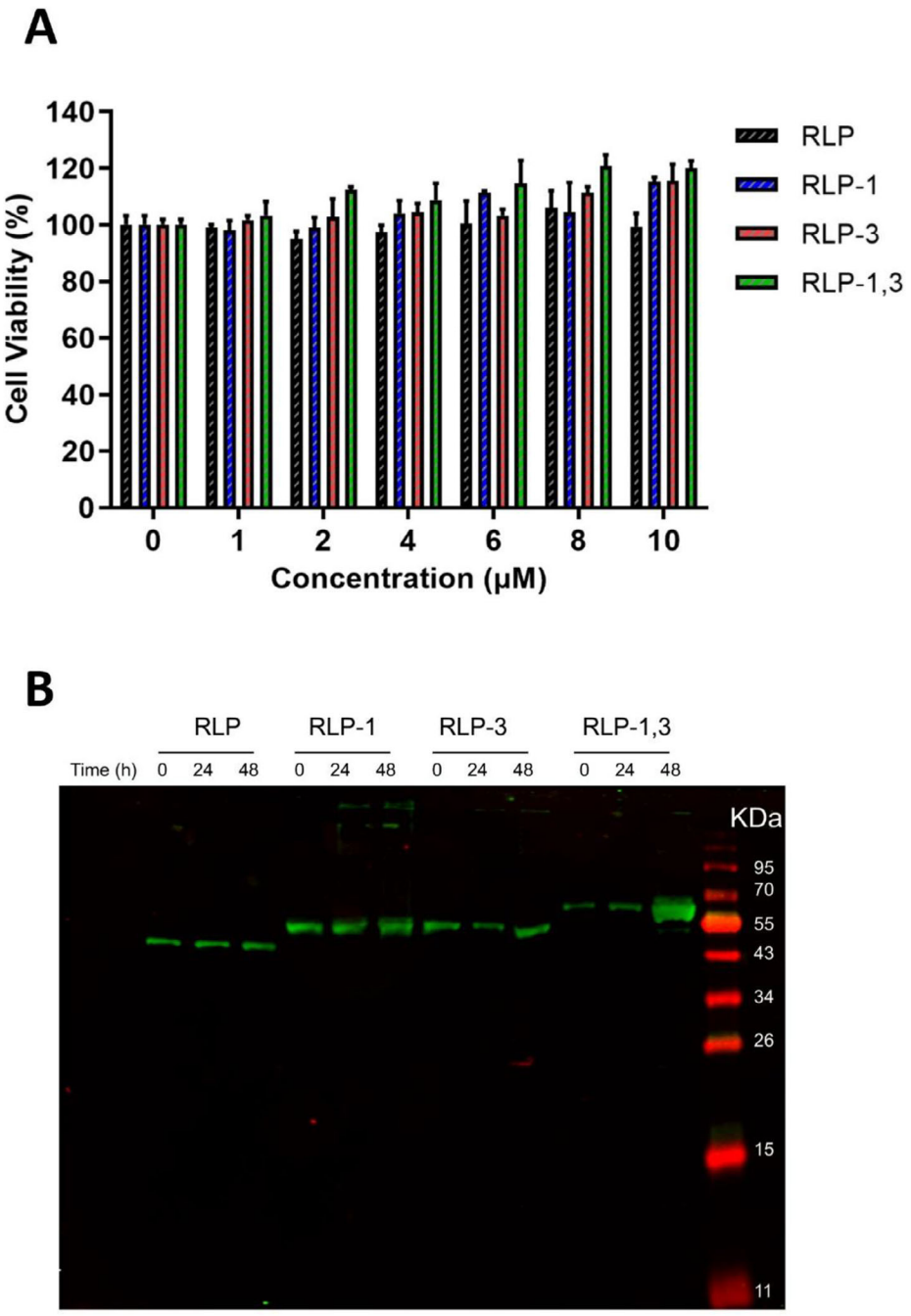

Figure 7. The RLPs are biocompatible and stable in human plasma. A) Cell viability of HeLa cells after 72 h of incubation with various concentrations of RLPs. Results are presented as mean ± SD (n = 3). B) Stability of the RLPs in human plasma assessed during 48 h by Western blot.

baseline-corrected values from 100) to those of control samples lacking RLP nanoparticles. The IC_{50} was determined by fitting acquired values to a non-linear regression curve using GraphPad Prism V6.01 (GraphPad Software, Inc., USA).

Virus Neutralization: Neutralization assays using Wuhan or Omicron BA.5 virus were performed by incubation of serial dilutions of the RLPs for 1 h at 37 °C in the presence of SARS-CoV-2 in Dulbecco's Modified Eagle Medium (DMEM) supplemented with 2% Fetal Bovine Serum (FBS). 50 µL of the mixtures were then added to Vero cells monolayers for an hour at 37 °C (MOI = 0.004). Infectious media were removed and replaced with DMEM containing 2% FBS. After 72 h, cells were fixed with paraformaldehyde (PFA) 4% (4 °C, 20 min) and stained with crystal violet solution in methanol. The cytopathic effect (CPE) of the virus on the cell monolayer was assessed visually, if even a minor damage to the monolayer (1–2 plaques) was observed in the well; this well was considered as a well with a manifestation of CPE. Neutralization titer was defined as the highest serum dilution without any CPE in two of three replicable wells. Otherwise, plates were scanned for determination of media absorbance at 585 nm, and non-linear curves were fitted to obtain the titer corresponding to the 50% of neutralization (NT_{50}) using GraphPad Prism V6.01 (Graph-

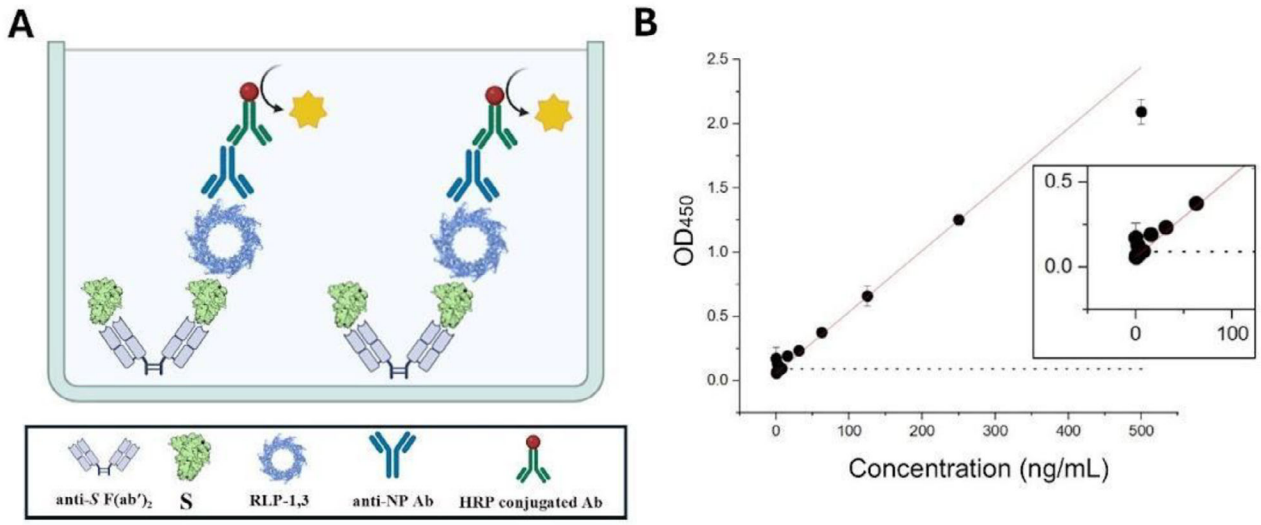

Figure 8. Schematic representation and results of the ELISA titration assay for SARS CoV-2 Spike protein. A) Schematic illustration of the ELISA setup used to evaluate binding of RLP-1,3 to the *S* protein. Figure created using BioRender.com. B) ELISA titration results expressed as absorbance at 450 nm (A_{450}) versus *S* concentration (ng/mL). Dotted line indicates the cut-off to set the titer calculated as the double of the negative control A_{450}.

Pad Software, Inc., USA). Neutralization assays to compare neutralization among the Wuhan and Omicron BA.5 variants were performed in the same plate for each sample.

Cytotoxicity Assay: HeLa cells (American Type Culture Collection, ATCC) were maintained in DMEM (Gibco, Invitrogen, USA) supplemented with 10% (v/v) FBS, and 1% penicillin-streptomycin at 37 °C in a humidified atmosphere with 5% CO_2. HeLa cells were seeded in 96-well microplates at a density of 3.5×10^3 cells per well. The microplates were maintained at 37 °C in a humidified atmosphere with 5% CO_2 for 24 h to allow cells to adhere to the culture microplates. Then, the RLPs were added at 1, 2, 4, 6, 8, and 10 µM to cells in triplicates and incubated for 72 h at 37 °C in a humidified atmosphere with 5% CO_2. Untreated cells, used as control, and blank wells, containing media only, were also included. After the incubation period, 10 µL of PrestoBlue reagent (Invitrogen) was added to each well, and the plate was incubated for an additional 15 min. Cell viability was determined by recording fluorescence emission at 615 nm, with an excitation wavelength at 531 nm, using a Victor III Multilabel Plate Reader (Perkin Elmer). Cell viability, expressed as a percentage relative to the control wells, was calculated using (Equation 2):

$$\text{Cell Viability (\%)} = \frac{(\text{Experimental well value} - \text{Blank well value})}{(\text{Control well value} - \text{Blank well value})} \times 100 \quad (2)$$

Stability of RLPs in Plasma: RLP nanoparticles were incubated in 100 µL of plasma at a final concentration of 16 µM in each of four 0.5 mL low-protein-binding microtube and maintained at 37 °C. Aliquots were taken at 0, 24, and 48 h, and 4x loading buffer was added to each sample, which was then immediately frozen at −20 °C until analysis.

For analysis, each sample was incubated at 90 °C for 5 min, and 12 µL (9.3 µM) of the heated sample was loaded onto a 15% SDS-PAGE gel. The proteins were electrophoretically transferred to a methanol-activated PVDF membrane (Immobilon-P Transfer Membranes, Merck Millipore, Germany) using a Trans-Blot Cell (Bio-Rad, China) in 1x Transfer Buffer (0.05 M Tris-HCl, 0.04 M glycine, 0.04% SDS, and 20% methanol) at 100 V for 1 h. The membrane was then blocked for 1 h in 1x TBST buffer containing 10% non-fat dried milk.

After blocking, the membrane was incubated overnight at 4 °C with a 1:1000 dilution of anti-His tag mouse monoclonal antibody (Genscript, Clone 6G2A9). The membrane was then washed with 1x TBST (3 × 10 min) and incubated for 1 h with a 1:20000 dilution of anti-mouse IgG conjugated to IRDye 800RD (LI-COR 926–68071). Fluorescent signals were captured using Odyssey Imaging System.

ELISA Assays: Plates were coated with 4 µg mL^{-1} anti-*S* horse $F(ab')_2$ overnight at 4 °C. The plates were then blocked with 3% BSA in TBS containing 0.05% Tween-20 (TBS-T) for 2 h at 37 °C and incubated with serial dilutions of recombinant Wuhan strain of *S* protein for 1 h at 37 °C. After incubation, the plates were washed with TBS-T and incubated 1 h at 37 °C with 0.5 µg mL^{-1} RLP-1,3, followed by mouse anti-*NP* antibody and then anti-mouse HRP-conjugated antibody. The plates were then washed, and the reactions were developed using tetramethylbenzidine (TMB) substrate. Absorbance values were recorded at 450 nm using a microplate reader. The titre was established as the minimum Spike concentration in which the measured absorbance was twice as high as that determined for the control group (without RLP-1,3).

Analysis of the Dynamics of the Nanoring: Coarse-grained molecular dynamics simulations were conducted using Sirah 2.2[56] and Gromacs 2022.4.[57] The oligomer was solvated in a box with a 2-nanometer margin on the sides of the initial model (≈22.5 nm) at a NaCl concentration of 0.15 M and a temperature of 300 K (27 °C). Residues in the scaffold were restrained, maintaining the overall original architecture. After running the simulation for 1.5 microseconds, the trajectory was analyzed using an in-house protocol. In summary, the trajectory was correctly oriented, and the horizontal distance between the center of mass of each binder (LCB1/LCB3) and the scaffold was calculated for each frame of the trajectory. To backmap the trajectory into an all-atom representation, we used cg2all.[58] Molecular graphics performed with UCSF ChimeraX.[59]

Statistical Analysis: All statistical analyses were performed using GraphPad Prism v6.01 (GraphPad Software, Inc., USA). For neutralization assays, non-linear regression (four-parameter logistic model) was applied to determine IC_{50} values. Global comparisons of neutralizers were conducted using the extra sum-of-squares F test, and pairwise analyses used to evaluate statistically significant differences. In both NanoLuc-based assays, neutralization potency was determined from a single experiment, with each concentration tested in duplicate. Data are reported as the mean of two technical replicates, with error bars indicating the standard deviation (SD).

Neutralization activity against Wuhan (A) and Omicron BA.5 (B) strains of SARS-CoV-2 was evaluated in an experiment consisting of three technical replicates. Results are represented as the mean of the replicates, with error bars indicating the standard deviation. Dose response curves

Table 3. SARS-CoV-2 neutralizing compounds based on established or emerging technologies.

Technology	IC_{50} (approx.)	Methodology	Modularity	Adaptability	Production system
RLPs (This Work)	RLP-1,3, IC_{50} (pseudovirus) 0.57 pM; NT_{50} (authentic virus, Wuhan) 0.23 nM; NT_{50} (Omicron BA.5) 1.19 nM	Binder-scaffold design → linker selection → expression and purification	Decameric ring-like particles that spontaneously self-assemble with plug-and-(dis)play capabilities	RLP scaffold with 20 anchor points for binder tethering. Efficacy against multiple strains.	E. coli Bl21 (DE3)
DARPins[50]	Monomers, ≈∼0.7–1 µM; Trimers, ≈0.3–1.8 nM (Wuhan-1), ≈7–8 pM (Omicron)	$>10^9$ DARPin library panning; trimerized via T4 foldon + flexible linkers	Monomers assembled into foldon-based trimers for potency boost	Reusable and re-engineerable for different variants	E. coli Bl21 (DE3)
Nanobodies[51]	Monomers ≤20 nM; Oligomers ≈100 pM	Llama immunization → VHH library → expression & oligomerization → RBD binder screening	Monomers covering multiple epitopes, assembled into cocktails / multimer	Reusable and flexible re-engineering for variants	Arctic Express (DE3) cells
AI-designed Nanobodies[52]	ELISA EC50 JN.1 ≈ 2.0 ng mL^{-1} (≈154 pM) vs Wuhan ≈ 0.2 ng mL^{-1} (≈15 pM)	AI pipeline (ESM → AlphaFold-Multimer → Rosetta) applied to 4 known nanobodies → in silico residue mutation to boost KP.3 RBD binding → wet-lab binding validation	Plug-and-play AI tool chain with interchangeable modules	Rapid retargeting to new pathogens/variants via AI-agent framework	E. coli periplasmic expression (nanobodies)
Double-stapled peptides (ACE2-helix decoy)[53]	Lowest IC_{50} ≈ 2 µM (NYBSP-4)	ACE2 contact helix (∼30 aa) → choose i/i+4–i+7 staple sites → assemble on Fmoc Rink-amide (MBHA) resin → form hydrocarbon staples on-resin → release from resin → ether precipitation/wash → HPLC	Staple repositioning on the ACE2 Helix-1 (resulted in four double-stapled peptides with different staple layouts)	Platform expected to enable optimization; activity against variants not evaluated	Chemical synthesis
Monoclonal antibody[54]	Most potent ≈ <67 pM; SARS2-38 ∼7–47 pM across VOCs/VOIs	Mouse immunization → hybridoma generation → screening for potent neutralizers → chimeric IgG1 expression	Mouse VH/VL were captured and re-cloned into human IgG1 heavy- and kappa light-chain vectors	Broad neutralization across multiple SARS-CoV-2 VOCs/VOIs (e.g., SARS2-38)	Hybridoma culture (serum-free) & Expi293 expression for chimeric IgG1

were fitted by nonlinear regression using a four-parameter logistic model (Figure 6). For all cases, viral entry inhibition was observed. EC_{50} values were obtained by curve fitting by nonlinear regression using a four-parameter logistic model, except for RLP-3 against the Omicron BA.5 that could not be fitted due to the low neutralizing potency observed.

DLS measurements obtained from an average of 30 consecutive runs, repeated five times per sample. Hydrodynamic diameters are reported as mean ± SD of these five measurements, while the polydispersity index (PDI) is presented as a representative value for each sample. Size analysis by TEM was carried out using ImageJ software (version 1.53e; National Institutes of Health, Bethesda, MD, USA), averaging 100 individual measurements per RLP nanoparticle across multiple grid regions. Values are expressed as mean ± SD.

Supporting Information

Supporting Information is available from the Wiley Online Library or from the author.

Acknowledgements

D.A.-P., S.E., D.H.M., and M.V.T. are CONICET staff members. C.G., C.A.P., and A.L.P. are CONICET fellows. S.V. is a UAB and I3PT-CERCA staff member. S.N. and J.P. are UAB staff members. M.B. and O.B. are UAB fellows supported by the Spanish Ministry of Science and Innovation via a doctoral grant (FPU22/03656, PRE2020-092634), respectively. Additionally, the authors express their gratitude to BioRender for providing tools used to create various images and illustrations (BioRender.com). The Agencia I+D+i, Argentina (PICTO-COVID-INMUNIZACION-0004, PICTA A CAT I 00008, and PICT 2020 SERIE A 00067), awarded to D.A.-P; Spanish Ministry of Science and Innovation (MICINN, Spain) (PID2022-137963OB-I00); ICREA (ICREA-Academia 2020, Spain); and the CERCA Programme of the Generalitat de Catalunya, awarded to S.V.

Conflict of Interest

The authors declare no conflict of interest.

Author Contributions

M.B., C.G., and S.E. optimized experimental protocols. C.G. and M.B. performed protein expression, purification and characterization, including structural, biocompatibility and neutralizing activity determinations. S.E., S.N., and D.A.-P. designed the constructs. O.B. performed the TMD

calculations. C.A.P., A.L.P. and M.V.T. generated polyclonal antibodies and characterized the diagnostics application of the constructs. All authors analyzed the data. M.B., C.G., J.P., D.A.-P., and S.V. wrote the manuscript. S.V. and D.A.-P. conceived the project and secured funding. All authors have given approval to the final version of the manuscript. M.B. and C.G. contributed equally to this work.

Data Availability Statement

The data that support the findings of this study are available from the corresponding author upon reasonable request.

Keywords

minibinders, protein scaffold, SARS-CoV-2, therapeutic, viral neutralization

Received: July 15, 2025
Revised: September 5, 2025
Published online:

[1] H. E. Davis, L. McCorkell, J. M. Vogel, E. J. Topol, *Nat. Rev. Microbiol.* **2023**, *21*, 133.
[2] M. Mariana, K. Rainer, *Oxford Rev. Economic Policy* **2020**, *36*, S256.
[3] M. I. Anasir, C. L. Poh, *Front. Microbiol.* **2019**, *10*, 738.
[4] B. S. Graham, M. S. A. Gilman, J. S. McLellan, *Annu. Rev. Med.* **2019**, *70*, 91.
[5] R. Rappuoli, E. De Gregorio, G. Del Giudice, S. Phogat, S. Pecetta, M. Pizza, E. Hanon, *Proc. Natl. Acad. Sci. USA* **2021**, *118*, 2020368118.
[6] E. de Wit, N. van Doremalen, D. Falzarano, V. J. Munster, *Nat. Rev. Microbiol.* **2016**, *14*, 523.
[7] L. Romina, P. M. Gonzalo, W. Diego, C. Silvina, B. Alejandra, B. Virginia, E. Ignacio, T. C. Mauricio, W. Cristian, B. Mabel, R. Aníbal, L. Gabriela, C. Pablo, R. Yvonne, F. V. Valeria, Á. P. Damián, E. Sebastián, F. Adrián, O. Gastón, C. Álvaro, R. Rocío, L. Jorge, V. Ricardo, I. Nicolás, H. Alejandra, O. M. Laura, E. Candela, N. Alejandra, N. Ivonne, A. Julieta, et al., *N. Engl. J. Med.* **2025**, *384*, 610.
[8] N. Visa, K. Chanice, E. Lise, H. Jussi, A. L. Abigail, P. T. Hoi, J. R. David, P. P. Fernando, S. Peter, H. Klaus, A.-P. Damian, H. Heli, *Oxford Academic* **2025**, *228*, 245.
[9] H. C, P. Y, P. V, C. Kl, E. Lj, M. I, S. Susanne, M. W. Erica, S.-O. Cynthia, Q. Zoe M, D. S. Christoph, J. M. Jakob, S. Miriam, S. Nicole, K. Nina, *The Cochrane Database Systemat. Rev.* **2022**, *6*.
[10] M. Tuccori, S. Ferraro, I. Convertino, E. Cappello, G. Valdiserra, C. Blandizzi, F. Maggi, D. Focosi, *mAbs* **2020**, *12*, 1854149.
[11] D. M. Weinreich, S. Sivapalasingam, T. Norton, S. Ali, H. Gao, R. Bhore, M. Bret, S. Yuhwen, R. Diana, I. Joseph, P. Christina, P. Cynthia, H. Romana, M. Adnan, D. D. John, C. T. Kenneth, T. H. Andrea, J. D. Hennifer, B. Alina, A. K. Christos, K. Yunji, A. C. Phar, R. Dip, K. Wendy, K. Anita, S. Yessica, G. Ximena, K. Bari, D. Thomas, S. Neil, et al., *The New Engl. J. Meds.* **2021**, *384*, 238.
[12] J. D. Lundgren, B. Grund, C. E. Barkauskas, T. L. Holland, R. L. Gottlieb, U. Sandkovsky, S. M. Brown, K. U. Knowlton, W. H. Self, D. C. Files, M. K. Jain, T. Benfield, M. E. Bowdish, B. G. Leshnower, J. V. Baker, J.-U. Jensen, E. M. Gardner, A. A. Ginde, E. S. Harris, I. S. Johansen, N. Markowitz, M. A. Matthay, L. Østergaard, C. C. Chang, V. J. Davey, A. Goodman, E. S. Higgs, D. D. Murray, T. A. Murray, R. Paredes, et al., *The New Engl. J. Med.* **2021**, *384*, 905.
[13] G. Lopardo, W. H. Belloso, E. Nannini, M. Colonna, S. Sanguineti, V. Zylberman, L. Muñoz, M. Dobarro, G. Lebersztein, J. Farina, G. Vidiella, A. Bertetti, F. Crudo, M. F. Alzogaray, L. Barcelona, R. Teijeiro, S. Lambert, D. Scublinsky, M. Iacono, V. Stanek, R. Solari, P. Cruz, M. M. Casas, L. Abusamra, H. L. Luciardi, A. Cremona, D. Caruso, B. de Miguel, S. P. Lloret, S. Millán, et al., *EClinicalMedicine* **2021**, *34*, 100843.
[14] D. H. Farizano Salazar, F. Achinelli, M. Colonna, L. Pérez, A. A. Giménez, M. A. Ojeda, M. P. N. Susana, N. Lía Sánchez, C. Florencia, M. I. I. Ornela, S. Santiago, S. Linus, A. G. Fernando, M. Carolina, R. Marta, P. Mariana, H. Yanina, Z. Vanesa, G. Sandra, K. Brenda, F. Francisco, D. Matías, R. Ian, H. G. Diego, N. Esteban, L. Gustavo, H. B. Waldo, *PLoS One* **2022**, *17*, 0274796.
[15] R. Shi, C. Shan, X. Duan, Z. Chen, P. Liu, J. Song, T. Song, X. Bi, C. Han, L. Wu, G. Gao, X. Hu, Y. Zhang, Z. Tong, W. Huang, W. J. Liu, G. Wu, B. Zhang, L. Wang, J. Qi, H. Feng, F.-S. Wang, Q. Wang, G. F. Gao, Z. Yuan, J. Yan, *Nature* **2020**, *584*, 120.
[16] Y. Wu, F. Wang, C. Shen, W. Peng, D. Li, C. Zhao, Z. Li, S. Li, Y. Bi, Y. Yang, Y. Gong, H. Xiao, Z. Fan, S. Tan, G. Wu, W. Tan, X. Lu, C. Fan, Q. Wang, Y. Liu, C. Zhang, J. Qi, G. F. Gao, F. Gao, L. Liu, *Science (New York, N.Y.)*. **2020**, *368*, 1274.
[17] X. Chi, R. Yan, J. Zhang, G. Zhang, Y. Zhang, M. Hao, Z. Zhang, P. Fan, Y. Dong, Y. Yang, Z. Chen, Y. Guo, J. Zhang, Y. Li, X. Song, Y. Chen, L. Xia, L. Fu, L. Hou, J. Xu, C. Yu, J. Li, Q. Zhou, W. Chen, *Science (New York, N.Y.)*. **2020**, *369*, 650.
[18] L. Liu, P. Wang, M. S. Nair, J. Yu, M. Rapp, Q. Wang, Y. Luo, J. F.-W. Chan, V. Sahi, A. Figueroa, X. V. Guo, G. Cerutti, J. Bimela, J. Gorman, T. Zhou, Z. Chen, K.-Y. Yuen, P. D. Kwong, J. G. Sodroski, M. T. Yin, Z. Sheng, Y. Huang, L. Shapiro, D. D. Ho, *Nature* **2020**, *584*, 450.
[19] S. J. Koussoroplis, G. Paulissen, D. Tyteca, H. Goldansaz, J. Todoroff, C. Barilly, C. Uyttenhove, J. Van Snick, D. Cataldo, R. Vanbever, *J. Controlled Release* **2014**, *187*, 91.
[20] A. Guillon, J. Pardessus, P. Lhommet, C. Parent, R. Respaud, D. Marchand, J. Montharu, M. De Monte, P. Janiak, C. Boixel, H. Audat, S. Huille, E. Guillot, N. Heuze-Vourc'h, *mAbs* **2019**, *11*, 297.
[21] L. Cao, I. Goreshnik, B. Coventry, J. B. Case, L. Miller, L. Kozodoy, R. E. Chen, L. Carter, A. C. Walls, Y.-J. Park, E.-M. Strauch, L. Stewart, M. S. Diamond, D. Veesler, D. Baker, *Science (New York, N.Y.)*. **2020**, *370*, 426.
[22] M. Popp, S. Reis, S. Schießer, R. I. Hausinger, M. Stegemann, M. I. Metzendorf, K. Peter, M. Patrick, S. Nicole, W. Stephanie, *The Cochrane Database Systemat. Rev.* **2022**, *6*, CD015017.
[23] R. Medhi, P. Srinoi, N. Ngo, H. V. Tran, T. R. Lee, *ACS Appl. Nano Mater.* **2020**, *3*, 8557.
[24] M. Behbahanipour, R. Benoit, S. Navarro, V. S. OligoBinders, *ACS Appl. Mater. Interfaces* **2023**, *15*, 11444.
[25] C. J. Goldin, R. Vázquez, F. P. Polack, D. Alvarez-Paggi, *Transl. Med. Commun.* **2020**, *5*, 15.
[26] M. Letko, A. Marzi, V. Munster, *Nat. Microbiol.* **2020**, *5*, 562.
[27] M. Hoffmann, H. Kleine-Weber, S. Schroeder, N. Krüger, T. Herrler, S. Erichsen, S. S. Tobias, H. Georg, W. Nai-Huei, N. Andreas, A. M. Marcel, D. Christian, P. Stefan, *Cell.* **2020**, *181*, p271.
[28] C. B. Jackson, M. Farzan, B. Chen, H. Choe, *Nat. Rev. Mol. Cell Biol.* **2022**, *23*, 3.
[29] F. Liu, X. Long, B. Zhang, W. Zhang, X. Chen, Z. Zhang, *J. Am. Gastroenterolog. Assoc.* **2020**, *18*, 2128.
[30] K. Nepali, R. Sharma, S. Sharma, A. Thakur, J. P. Liou, *J. Biomed. Sci.* **2022**, *29*, 65.
[31] Y. C. Lin, W. Y. Chen, E. T. Hwu, W. P. Hu, *Int. J. Mol. Sci.* **2022**, *23*, 5810.
[32] D. Alvarez Paggi, S. A. Esperante, M. Salgueiro, G. Camporeale, G. A. P. de Oliveira, G. Prat Gay, *Arch. Biochem. Biophys.* **2019**, *671*, 77.
[33] A. Jain, G. F. Trindade, J. M. Hicks, J. C. Potts, R. Rahman, R. J. M. Hague, D. B. Amabilino, L. Pérez-García, F. J. Rawson, *J. Colloid Interface Sci.* **2021**, *587*, 150.

[34] P.-L. Hervé, M. Raliou, C. Bourdieu, C. Dubuquoy, A. Petit-Camurdan, N. Bertho, J.-F. Eléouët, C. Chevalier, S. Riffault, *J. Virol.* **2014**, *88*, 325.
[35] C. Leyrat, F. Yabukarski, N. Tarbouriech, E. A. Ribeiro, M. R. Jensen, M. Blackledge, R. W. H. Ruigrok, M. Jamin, *PLoS Pathog.* **2011**, *7*, 1002248.
[36] R. N. Kirchdoerfer, D. M. Abelson, S. Li, M. R. Wood, E. O. Saphire, *Cell Rep.* **2015**, *12*, 140.
[37] R. G. Tawar, S. Duquerroy, C. Vonrhein, P. F. Varela, L. Damier-Piolle, N. Castagné, K. MacLellan, H. Bedouelle, G. Bricogne, D. Bhella, J.-F. Eléouët, F. A. Rey, *Science* **2009**, *326*, 1279.
[38] A. C. Hunt, J. B. Case, Y.-J. Park, L. Cao, K. Wu, A. C. Walls, Z. Liu, J. E. Bowen, H.-W. Yeh, S. Saini, L. Helms, Y. T. Zhao, T.-Y. Hsiang, T. N. Starr, I. Goreshnik, L. Kozodoy, L. Carter, R. Ravichandran, L. B. Green, W. L. Matochko, C. A. Thomson, B. Vögeli, A. Krüger, L. A. VanBlargan, R. E. Chen, B. Ying, A. L. Bailey, N. M. Kafai, S. E. Boyken, A. Ljubetic, et al., *Sci. Transl. Med.* **2022**, *14*, abn1252.
[39] J. Alves, L. Engel, R. de Vasconcelos Cabral, E. L. Rodrigues, L. de Jesus Ribeiro, L. M. Higa, O. da Costa Ferreira Júnior, T. M. P. P. Castiñeiras, I. de Carvalho Leitão, A. Tanuri, S. A. Goueli, H. Zegzouti, *Sci. Rep.* **2021**, *11*, 18428.
[40] E. Qing, T. Kicmal, B. Kumar, G. M. Hawkins, E. Timm, S. Perlman, T. Gallagher, *mBio* **2021**, *12*, 0159021.
[41] E. Qing, P. Li, L. Cooper, S. Schulz, H.-M. Jäck, L. Rong, S. Perlman, T. Gallagher, *Cell Rep.* **2022**, *39*, 110786.
[42] L. Zuo, G. Ao, Y. Wang, M. Gao, X. Qi, *The Journal of Infection* **2022**, *84*, 248.
[43] *Lancet (London, England)*. **2022**, *399*, 665.
[44] R. L. Gottlieb, A. Nirula, P. Chen, J. Boscia, B. Heller, J. Morris, G. Huhn, J. Cardona, B. Mocherla, V. Stosor, I. Shawa, P. Kumar, A. C. Adams, J. Van Naarden, K. L. Custer, M. Durante, G. Oakley, A. E. Schade, T. R. Holzer, P. J. Ebert, R. E. Higgs, N. L. Kallewaard, J. Sabo, D. R. Patel, P. Klekotka, L. Shen, D. M. Skovronsky, *JAMA, J. Am. Med. Assoc.* **2021**, *325*, 632.
[45] M. Falcone, G. Tiseo, B. Valoriani, C. Barbieri, S. Occhineri, P. Mazzetti, M. L. Vatteroni, L. R. Suardi, N. Riccardi, M. Pistello, D. Tacconi, F. Menichetti, *Infectious Diseases and Therapy* **2021**, *10*, 2479.
[46] M. Díaz-Caballero, S. Navarro, S. Ventura, *Biomacromolecules* **2020**, *21*, 2334.
[47] BOLETIN OFICIAL REPUBLICA ARGENTINA-MINISTERIO DE SALUD SECRETARÍA DE CALIDAD EN SALUD-Resolución 8/2021, https://www.boletinoficial.gob.ar/detalleAviso/primera/240178 [Accessed 11th September **2023**].
[48] G. N. Llewellyn, H.-Y. Chen, G. L. Rogers, X. Huang, P. J. Sell, J. E. Henley, P. M. Cannon, *J. Virol.* **2023**, *97*, 0068423.
[49] GENLISA Human SARS-CoV-2 Spike S1 Protein Antigen ELISA Kit. Krishgen Biosystems, https://krishgen.com/product/details/human-sars-cov-2-spike-s1-protein-antigen-elisa-quantitative/[Accessed 11th June **2025**].
[50] V. Chonira, Y. D. Kwon, J. Gorman, J. B. Case, Z. Ku, R. Simeon, R. G. Casner, D. R. Harris, A. S. Olia, T. Stephens, L. Shapiro, M. F. Bender, H. Boyd, I.-T. Teng, Y. Tsybovsky, F. Krammer, N. Zhang, M. S. Diamond, P. D. Kwong, Z. An, Z. Chen, *Nat. Chem. Biol.* **2023**, *19*, 284.
[51] Highly synergistic combinations of nanobodies that target SARS-CoV-2 and are resistant to escape-PubMed, https://pubmed.ncbi.nlm.nih.gov/34874007[Accessed 1st September **2025**].
[52] K. Swanson, W. Wu, N. L. Bulaong, J. E. Pak, J. Zou, *Nature* **2025**, 1.
[53] F. Curreli, S. M. B. Victor, S. Ahmed, A. Drelich, X. Tong, C.-T. K. Tseng, C. D. Hillyer, A. K. Debnath, *mBio* **2020**, *11*, 02451.
[54] A potently neutralizing SARS-CoV-2 antibody inhibits variants of concern by utilizing unique binding residues in a highly conserved epitope-PubMed, https://pubmed.ncbi.nlm.nih.gov/34481543.[Accessed 1st September **2025**].
[55] J. Z. Porterfield, A. Zlotnick, *Virology* **2010**, *407*, 281.
[56] F. Klein, M. Soñora, S. L. Helene, F. E. Nazareno, A. Ballesteros-Casallas, M. M. Rodrigo, S. Pantano, *J. Struct. Biol.* **2023**, *215*, 107985.
[57] M. J. Abraham, T. Murtola, R. Schulz, S. Páll, J. C. Smith, B. Hess, E. Lindahl, *SoftwareX* **2015**, *1*, 19.
[58] L. Heo, M. Feig, One bead per residue can describe all-atom protein structures. Structure (London, England: 1993). **2024**, *32*, 97–111.e6, https://doi.org/10.1016/j.str.2023.10.013.
[59] C. M. Elaine, D. G. Thomas, F. P. Eric, S. C. Greg, J. P. Zach, H. M. John, E. F. Thomas, *Wiley Online Library* **2025**, *32*, 4792.